

1 **Gravity wave induced instability of the stratospheric polar vortex edge**

2 Lawrence Coy,^{a,b} Paul A. Newman,^a William M. Putman,^a Steven Pawson,^a and
3 M. Joan Alexander^c

4 ^a*NASA GSFC, Greenbelt, MD, USA*

5 ^b*SSAI, Lanham, MD, USA*

6 ^c*NWRA, Boulder, CO, USA*

7 *Corresponding author:* Lawrence Coy, lawrence.coy@nasa.gov

8 ABSTRACT: We report on a previously undocumented process capable of mixing Northern Hemi-
9 sphere (NH) winter Ertel potential vorticity (EPV)—instabilities introduced along the stratospheric
10 polar vortex edge by breaking gravity waves (GWs). As horizontal resolution has increased, global
11 scale atmospheric models and data assimilation systems (DAS) are now able to capture some
12 aspects of GW generation, propagation, and dissipation, as well as mesoscale EPV disturbances.
13 This work examines resolved GWs, their breaking, and their interaction with the stratospheric polar
14 vortex as seen in the NASA Global Modeling and Assimilation Office DAS during the 2021–2022
15 NH winter. This analysis shows that tropospheric generated GWs, breaking in the stratosphere
16 over a substantial area, created a significant disruption of the polar vortex EPV, in turn trigger-
17 ing baroclinic instabilities near the edge of the polar vortex. The instabilities take the form of
18 mesoscale vortices propagating on the edge of the stratospheric polar vortex. This work reveals
19 two new features in the EPV analysis: high and low fluctuations at the smallest model scale created
20 by resolved GW breaking, and high values associated with mesoscale vortices along the edge of
21 the polar vortex.

22 SIGNIFICANCE STATEMENT: The northern hemisphere (NH) winter stratospheric polar vor-
23 tex is typically disturbed by global scale waves that displace, distort, and weaken the vortex,
24 however, as the resolution of global models has increased, the role played by smaller scale waves
25 in disturbing the stratospheric vortex can now be evaluated. As one example, the NH winter of
26 2022 had unusually weak global scale waves along with strong smaller scale waves generated by
27 flow over mountains, providing an ideal case for evaluating the effects brought about by the smaller
28 scale waves. Our examination of the 2022 NH winter reveals that the waves generated by flow over
29 mountains, located under the stratospheric vortex, propagated up to the middle stratosphere where
30 they broke down, interfering significantly with the vortex flow. This distortion of the vortex flow
31 created an unstable region that led to the formation of “mesoscale vortices”, relatively small eddies
32 on the edge of the polar vortex, that then propagated coherently around the stratospheric vortex.
33 The importance of these, small scale wave generated, mesoscale vortices may lie in their potential
34 to mix trace gases across the stratospheric vortex boundary.

35 **1. Introduction**

36 Past studies of the stratosphere have emphasized the importance of Ertel’s potential vorticity
37 (EPV) as a well conserved dynamical tracer (Hoskins et al. 1985). These early studies often
38 dealt with limited horizontal resolution making the identification of important global EPV features
39 remarkable at the time. For Example, McIntyre and Palmer (1983) characterized the EPV fields
40 used in their discovery of breaking planetary waves as “. . . resembling a blurred view of reality seen
41 through a pane of knobbly glass . . .”. This “knobbly glass” has been smoothed considerably over
42 the following decades based on data assimilation techniques in conjunction with high horizontal
43 resolution global models. Indeed, recent data assimilation reanalysis of the McIntyre and Palmer
44 (1983) breaking wave examples provides dynamically consistent confirmations of their breaking
45 planetary wave discovery (Butchart 2022).

46 While the planetary scale waves are well resolved in modern EPV fields, the question arises
47 as to the possibility of increased model resolution leading to new discoveries. That is, can
48 “magnification” of current EPV fields provide further insights into stratosphere and mesosphere
49 dynamics. Here we investigate two new features resulting from increased horizontal resolution:

50 signatures of breaking gravity waves (GW) followed by the formation of mesoscale vortices on the
51 polar vortex edge.

52 The Northern Hemisphere (NH) stratospheric polar vortex forms every winter, however, consid-
53 erable vortex variability exists, especially in years with stratospheric sudden warmings (SSWs).
54 During SSW events, high EPV in the stratospheric polar vortex is mixed down to lower latitudes
55 by global-scale planetary waves. The planetary waves are said to be “breaking” when they create
56 regions where the latitudinal EPV gradient is reversed and these reversed gradient regions can lead
57 to instabilities in the wave breaking region (see Butchart 2022, and references therein).

58 Here we report on another process capable of mixing NH winter EPV—instabilities introduced
59 along the polar vortex edge by breaking gravity waves (GW). GWs are generated by flow over
60 orography, convection, fronts, or flow instabilities (Alexander 2010). Their successful vertical
61 propagation depends on the background atmospheric flow. Under the right conditions GWs can
62 transfer significant momentum and energy from the troposphere to the middle atmosphere. As
63 vertically propagating GWs encounter lower densities or approach a critical layer, they increase
64 in amplitude until they become unstable and “break”, depositing momentum and energy to the
65 background flow and hence providing the possibility of disrupting the winter stratospheric polar
66 vortex. Parameterizations of this GW momentum drag attempt to capture these effects, playing a
67 major role in the upper stratosphere momentum budget and a significant role in some SSW events
68 (Albers and Birner 2014; Achatz et al. 2024).

69 As noted above, global scale atmospheric models and data assimilation systems (DAS) routinely
70 resolve the main features of the stratospheric polar vortex along with planetary wave variability and
71 breaking. As the horizontal resolution has increased over time these models are now able to capture
72 convective systems and some aspects of GW generation, propagation, and dissipation (Watanabe
73 and Miyahara 2009; Holt et al. 2017; Stevens et al. 2019; Shibuya and Sato 2019; Okui et al. 2023).
74 Here we report on resolved GWs, their breaking, and their interaction with the stratospheric polar
75 vortex as seen in the NASA Global Modeling and Assimilation Office (GMAO) near real time
76 forward processing (FP) system during the 2021–2022 NH winter.

77 Our plan is to examine a somewhat atypical NH winter (2021–2022), where planetary wave
78 activity was relatively weak and the stratospheric polar vortex strong, allowing GWs to dominate
79 the polar vortex disturbances. The working hypothesis is that orographically generated GWs,

80 breaking in the mid-to upper stratosphere, distorted the edge of the polar vortex, creating regions
81 of unstable EPV gradients. These in turn generated a series of what will be called here mesoscale
82 vortices, incorporating signatures of latitudinal mixing, on the edge of the polar vortex.

83 The process of longitudinally localized GWs acting to generate larger-scale, planetary waves
84 has been observed and modeled in the mesosphere (Smith 1996; Siskind et al. 2010; Matthias and
85 Ern 2018; Sato et al. 2018). These studies demonstrate the ability of GWs to make significant
86 changes at larger scales. Here we extend these studies to examine the role of GWs in the creation of
87 mesoscale vortices near the edge of the stratospheric polar vortex using a high horizontal resolution
88 data assimilation system.

89 As will be shown below, the mesoscale vortices generated by the breaking GWs developed
90 centers with extremely high EPV. While EPV is often well conserved in the stratosphere (Haynes
91 and McIntyre 1990), diabatic and frictional forces can change the EPV of an air parcel (Haynes and
92 McIntyre 1987) and such non-conservation processes must be occurring here. The development
93 and propagation of the high EPV mesoscale vortices will be documented below, however, a detailed
94 EPV budget is left for future studies.

95 In the following, Section 2 provides a description of the DA systems and models used. The
96 main DAS is the NASA GEOS (Global Earth Observing System) FP system, however some lower
97 horizontal resolution MERRA-2 (Modern-Era Retrospective analysis for Research and Applica-
98 tions) output is included for comparison. To investigate the potential for baroclinic instability near
99 the polar vortex edge, results are presented from a linear quasi-geostrophic beta plane model, also
100 described in Section 2. The results are presented in Section 3, with subsections on the 2021-2022
101 NH winter, the resolved GWs, the structure of the mesoscale vortices, dependence on resolution,
102 and the linear instability model. A summary of the results along with conclusions are presented in
103 Section 4.

104 **2. Global Assimilation Products and Data**

105 *a. GEOS FP System*

106 The NASA GMAO GEOS FP DAS routinely produces global, near-real-time, meteorological
107 analysis fields and forecasts available at three hourly intervals. This system updates frequently
108 (approximately every six months) to better incorporate new data types and the latest model de-

109 velopments. The DAS utilizes a full suite of observation types including aerosol, temperature,
110 pressure, radiances, winds, moisture, radio occultation, and ozone measurements. Each six hourly
111 analysis assimilates roughly two million observations. Zhu et al. (2022) provides a current descrip-
112 tion of the GEOS DAS.

113 The system used during the NH winter of 2021–2022 was run at ~ 12 km horizontal resolution
114 on a cubed sphere grid (Putman and Lin 2007) with meteorological fields saved on a $5/16$ by $1/4$
115 degree longitude by latitude horizontal grid and on either the full 72 model levels (model top at
116 0.01 hPa) or vertically interpolated to 42 pressure levels. A description of the model physics can be
117 found in Arnold et al. (2020). The most recent two weeks of forecasts are available on the NASA
118 Center for Climate Simulation (NCCS) data portal. The specific archived analysis fields used in
119 the study are available as described in the Open Research Section.

120 Taking the horizontal grid resolution for GEOS FP as ~ 12.5 – 14 km and the system’s effective
121 resolution as $\sim 7\times$ the grid resolution, yields ~ 87.5 – 98 km as the effective system resolution.
122 The width of the Scandinavian ridge is about 300 km while the gravity waves resolved waves
123 examined below have a horizontal scale of ~ 300 – 500 km, both well within the effective resolution
124 of GEOS FP.

125 To investigate the dependence on horizontal resolution, EPV fields are shown from a test DAS
126 (x0048) run at half the GEOS FP system resolution (24 km). While the GEOS FP ($\sim 1/8$ degree)
127 and the test system ($\sim 1/4$ degree) are run with different horizontal resolutions, the results are saved
128 on the same output grid. Note that the MERRA-2 system ($\sim 1/2$ degree), described below, is also
129 included in the resolution comparisons.

130 *b. MERRA-2*

131 The MERRA-2 system provides ongoing global atmospheric reanalyses starting in 1980. Unlike
132 the FP system, the MERRA-2 system is frozen, with only the input data changing with time. The
133 MERRA-2 vertical levels are the same as in FP, however MERRA-2, with fields saved at $5/8$ by
134 $1/2$ degree longitude by latitude, has more coarse horizontal resolution than FP. An overview of
135 MERRA-2 is given by Gelaro et al. (2017). Here we used the monthly averaged pressure level
136 fields (GMAO 2015b) when comparing the NH winter 2022 climate with other winters and the

137 instantaneous model level EPV fields (GMAO 2015a) when comparing specific time EPV fields
138 between FP and MERRA-2.

139 *c. Linear Instability Model*

140 The potential for baroclinic instability near the disturbed vortex edge is investigated using a
141 quasi-geostrophic, beta-plane, linear instability model. This is the same model used and described
142 in McCormack et al. (2014) and is based on the adiabatic and frictionless, linearized potential
143 vorticity equation (see Andrews et al. 1987, equation 3.4.5 and following equations):

$$q'_t + \bar{u}q'_x + v'\bar{q}_y = 0. \quad (1)$$

144 where q is quasi-geostrophic potential vorticity, u and v are the longitudinal and meridional velocity
145 components, and x , y , t , are the longitudinal and meridional directions and time. The overbars
146 denote a zonal average and the primes the deviation from a zonal average. Since q' and v' depend
147 linearly on the geostrophic stream function, ψ , assuming a wave solution for ψ with phase speed
148 c and zonal wavenumber k allows the x and t derivatives to be evaluated. With \bar{u} and \bar{q}_y then
149 specified as the environment to be tested for instability, and suitable boundary conditions, Eq. 1
150 can be finite differenced for a chosen value of k as:

$$\mathbf{A}\psi = c\mathbf{B}\psi \quad (2)$$

151 where the matrix, \mathbf{A} , depends on \bar{u} and \bar{q}_y , the matrix, \mathbf{B} , depends on the Laplacian operator, and
152 ψ is the vector of stream function values at each point in the two dimensional, latitude and altitude,
153 domain being investigated.

154 Eq. 2, can be solved for ψ and c , using standard routines. For simplicity we assume that the
155 instability is located far enough from the latitude and altitude domain boundaries that we can take ψ
156 equal to zero on all boundaries. Examination of the imaginary part of c allows for the identification
157 of the fastest growing mode structure, ψ , for each value of k specified.

158 *d. AIRS data*

159 For confirmation of the DAS resolved GWs we examined the GW signature found in the AIRS
160 (Atmospheric Infrared Sounder on the NASA Aqua satellite) $4.3 \mu\text{m}$ brightness temperature signal.
161 Horizontal resolution is 13.5 km at the nadir point below the satellite, similar to the resolution
162 of the FP system, and resolution decreases toward the measurement swath edges so that the
163 average resolution is ~ 20 km. The data are low-noise multi-channel averages with weighting
164 functions that peak between 30–40 km altitude (Hoffmann et al. 2014). Brightness temperature
165 wave anomalies are attenuated relative to sensible temperature anomalies, with attenuation that
166 is inversely proportional to vertical wavelength. These channels are most sensitive to the longer
167 vertical wavelength (≥ 15 km) GWs and are not expected to highlight wave breaking regions where
168 the vertical wavelength decreases. Note also that selected AIRS channels are assimilated in the
169 DAS so that the AIRS observations shown here are not entirely independent of the data assimilation
170 output, nevertheless, the AIRS observations shown here can be regarded as an independent analysis
171 of the GWs in the FP system forecasts.

172 **3. Results**

173 *a. The 2021–2022 Northern Hemisphere Winter Stratosphere*

174 The zonal mean of the zonal wind component at 10 hPa, 60°N provides a useful measure of
175 polar vortex strength that can be used to characterize the NH winter stratosphere. Winters with
176 high seasonally averaged DJF (December, January, February) winds either lack SSWs or have them
177 occurring late in the winter season. The 2021–2022 NH winter had the largest mean seasonal wind
178 seen in the 1980–2023 MERRA-2 time period, with a mean seasonal wind of 46.3 ms^{-1} , more than
179 1.5 standard deviations above the average value of 30.3 ms^{-1} .

180 As with the winds, the planetary-scale wave forcing from the troposphere can be considered over
181 the DJF season and variability is expected depending on interannual tropospheric variability. Here
182 we consider the zonally averaged meridional heat flux at 100 hPa and 60°N as a measure of the wave
183 forcing of the stratosphere. The NH 2021–2022 winter season had the lowest meridional heat flux
184 seen in the 1980–2023 MERRA-2 time period, with a mean seasonal heat flux of 17.2 Kms^{-1} , more
185 than 2 standard deviations below the average value of 24.3 Kms^{-1} . The record low 2021–2022
186 planetary-scale wave forcing at 100 hPa and 60°N is consistent with the strong stratospheric winds.

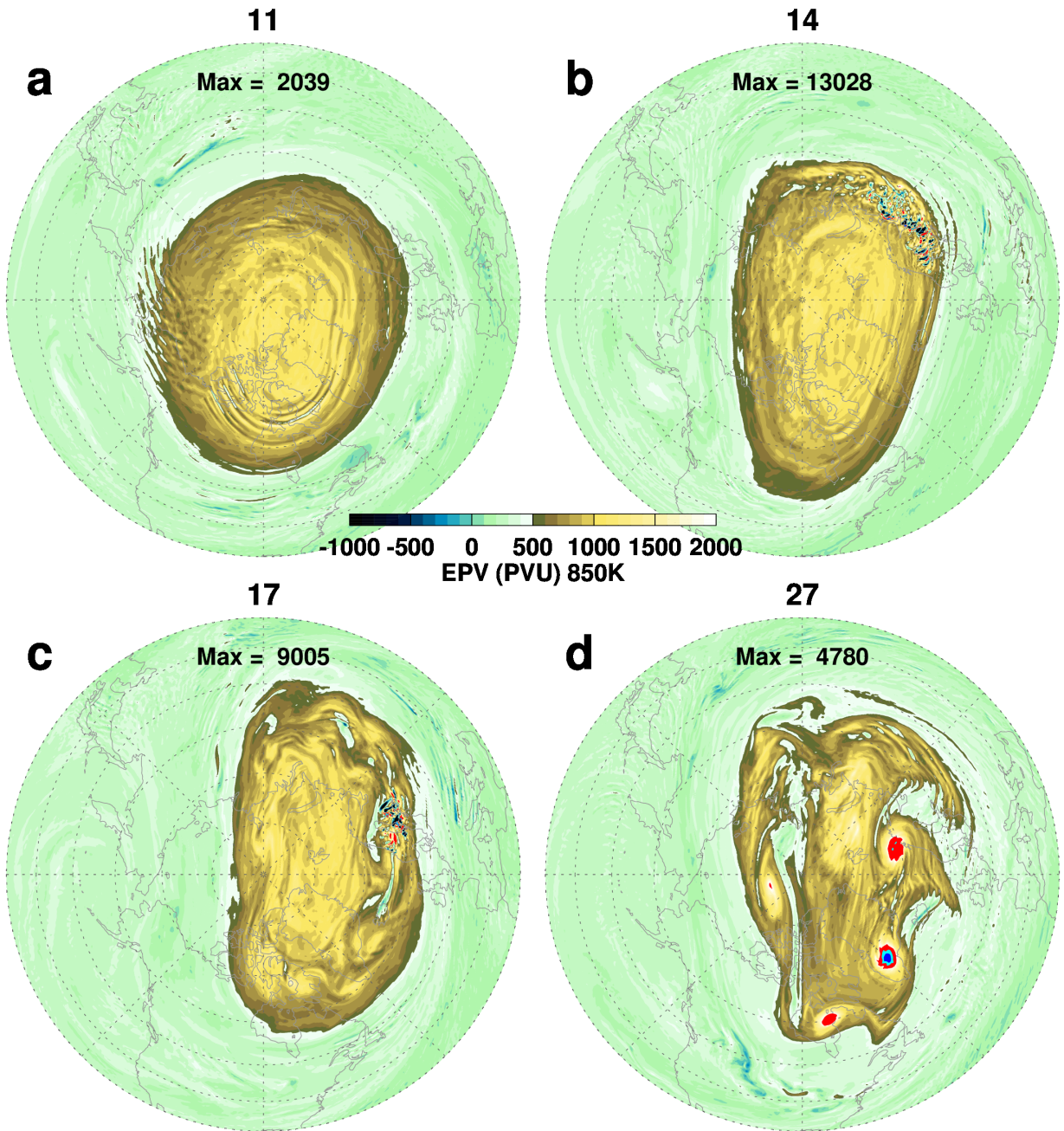
187 The strong winds and low wave forcing conjure up a picture of an undisturbed zonally symmetric
188 polar vortex. Nevertheless, the January 2022 stratospheric polar vortex transformed from a zonally
189 symmetric high Ertel potential vorticity (EPV) configuration (Fig. 1a) on 11 January to a much
190 more disturbed vortex (Fig. 1d) on 27 January. While there is an overall elongation of the 27 January
191 high EPV region, the most striking features are the ragged edge of the vortex (the high EPV region)
192 and the existence of four very high, localized EPV mesoscale vortices along the polar vortex edge.
193 On 11 January the maximum 850K EPV was $\sim 2,000$ PVU while by 27 January the maximum had
194 more than doubled to 4,780 PVU with the highest values associated with the strong EPV mesoscale
195 vortex at 45°W .

200 *b. Resolved gravity waves*

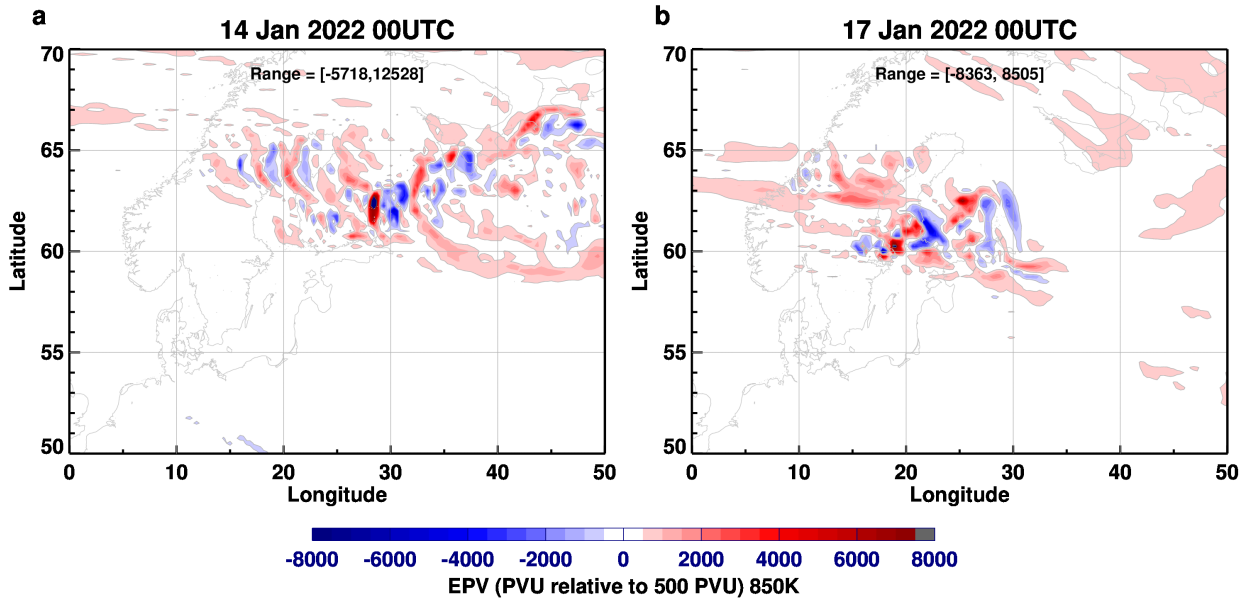
201 Between 11 and 27 January 2022 small regions of extremely high and low EPV values occurred
202 along the vortex edge, especially over Northern Europe with a maximum value of over 13,000 PVU
203 on 14 January (Fig. 1b). The polar vortex edge distorted in response to these perturbations, creating
204 separation of the high EPV from the main vortex on 14 January from 0° – 135°E . By 17 January,
205 the vortex edge became even more distorted as the high and low EPV perturbations continued
206 occurring over Northern Europe (Fig. 1c).

207 Looking more closely at the 850K EPV on 14 and 17 January (Fig. 2), alternating regions of
208 high and low EPV are seen near the polar vortex edge. The EPV values at these times are as much
209 as 8,000 PVU below and 12,500 PVU above the polar vortex edge value. On the 14th (Fig. 2a) a
210 high EPV feature is seen equatorward and then east of the disturbance region corresponding to the
211 EPV filament identified in Fig. 1b.

215 That these small-scale EPV disturbances are related to resolved GWs can be seen in the undula-
216 tions in the height of the 850K potential temperature surface (Fig. 3). The GWs in the height field
217 do not disturb the entire EPV field, as non-dissipating GWs should not be visible in the EPV field,
218 however, the EPV field is disturbed in the more northern part of the GW field where the GWs are
219 likely breaking in a non-EPV conserving manner. Note that the EPV varies on a smaller scale than
220 the scale of the GWs seen in the potential temperature surface oscillations and furthermore that the
221 orientation of the EPV oscillations differs from the orientation of the GWs. This relation between
222 the GW signature and the scale and orientation of the small-scale EPV field is consistent with 3D



196 FIG. 1. EPV on the 850K potential temperature surface for a) 11, b) 14, c) 17 and d) 27 January 2022 in
 197 potential vorticity units (PVU) where one PVU is equal to $10^{-6}m^2s^{-1}Kkg^{-1}$. The high EPV values are: red:
 198 2000–3000 PVU, cyan: 3000–4000 PVU, blue: 4000–5000 PVU, and yellow: above 5000 PVU. The vortex edge
 199 on 11 January 2022 is located at 500 PVU based on the method of Nash et al. (1996).

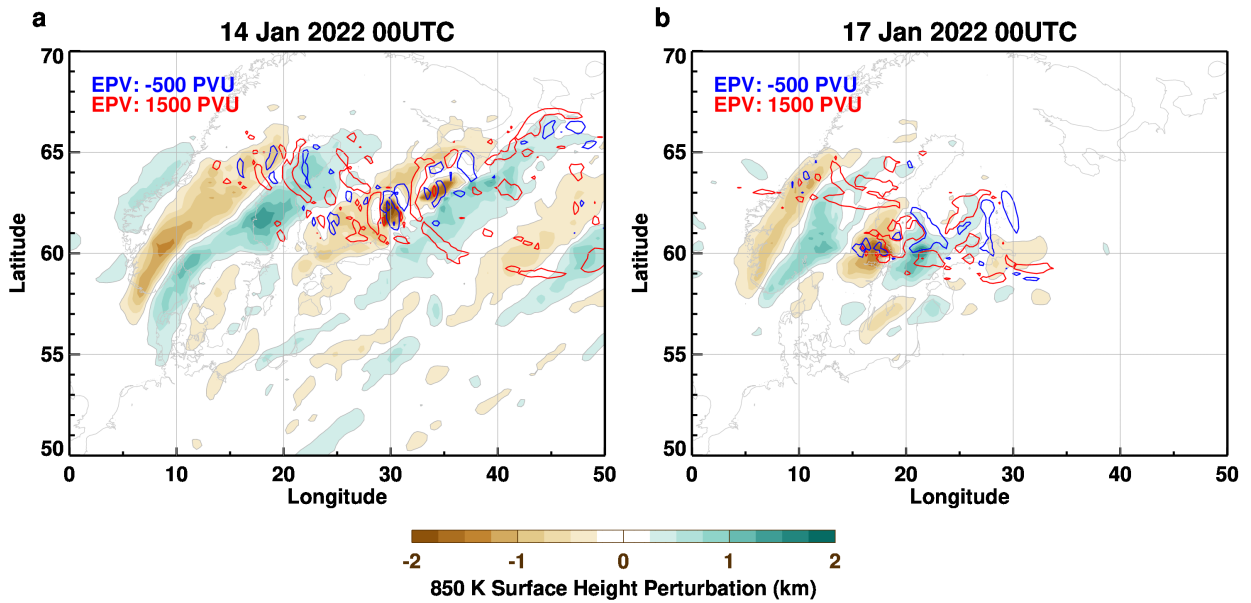


212 FIG. 2. Latitude (50-70°N) longitude (0°-50°E) projection of EPV on the 850K potential temperature surface
 213 for a) 14 January 2022 and b) 17 January 2022. The EPV contours are relative to 500 PVU, the value defining
 214 the vortex edge on 11 January 2022.

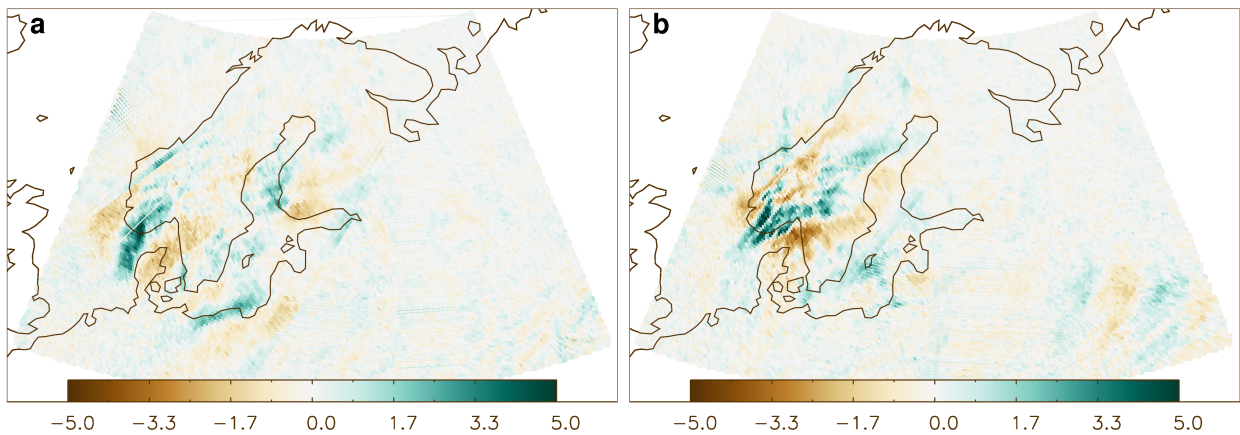
223 shear instability model studies of GW breaking and with GW observations (Fritts and Alexander
 224 2003, and references therein).

228 These model resolved GWs can also be seen directly in the AIRS observations (Fig. 4). These
 229 wave patterns highlight regions over southern Scandinavia where the strong GWs have the largest
 230 vertical wavelengths. Note that these brightness temperatures correspond well with the regions
 231 of potential temperature height surface variations shown in Fig. 3. In the regions where EPV
 232 fluctuations are large the AIRS GW signal is weak. This is more evidence that the EPV fluctuations
 233 characterize regions where GWs are breaking and hence have small vertical wavelengths there.

238 The vertical cross sections of potential temperature and zonal wind on 14 and 17 January (Fig. 5)
 239 highlight the stratospheric breaking wave region, topped by the strong easterly vertical wind shear
 240 and reversal of the zonal wind direction near the stratopause that inhibits the vertical propagation
 241 of orographic GWs. Thus the GWs are required to break in the stratosphere at this time. On both
 242 the 14th and the 17th the strong stratospheric westerlies at 10°W are reduced after crossing the
 243 GW region and are much weaker at 50°E than at 10°W, qualitatively consistent with an expected
 244 reduction of the zonal wind created by breaking GWs in the upper stratosphere. Nearly vertical

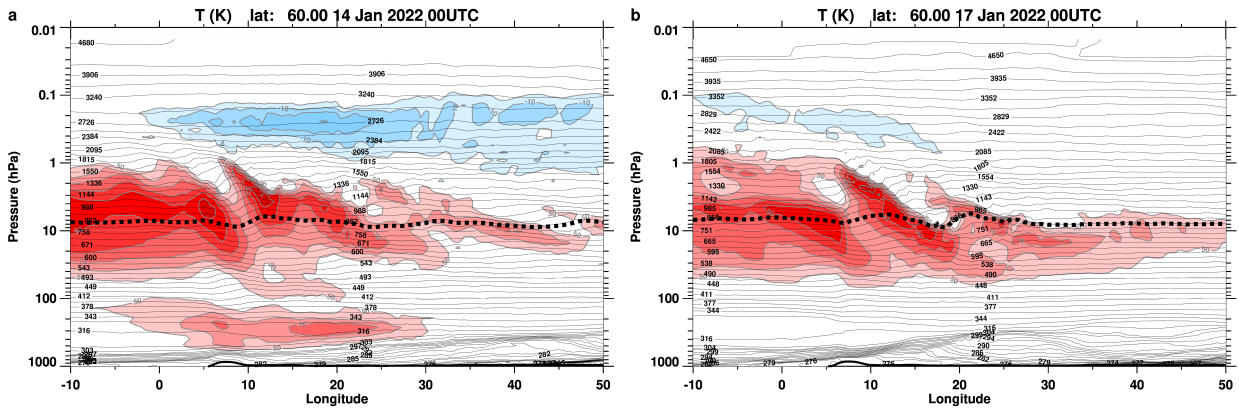


225 FIG. 3. Latitude (50-70°N) longitude (0°W-50°E) projection of the height of the 850K potential temperature
 226 surface (filled contours) and the -500 (blue) and 1500 (red) PVU contours on a) 14 January 2022 and b) 17
 227 January 2022.



234 FIG. 4. AIRS 4.3 μm brightness temperature anomalies on descending (nighttime) overpasses on a) 14 January
 235 and b) 17 January showing large amplitude mountain waves over southern Scandinavia. The UT times listed
 236 are the overpass times that cover the mountain waves. These are low-noise multi-channel averages described in
 237 Hoffmann et al. (2014) with weighting functions that peak between 30-40 km altitude.

245 potential temperature surfaces are also found on both the 14th and 17th (Fig. 5) indicating breaking



248 FIG. 5. Longitude (10°W–50°E) altitude (1000–0.01 hPa) cross section at 60°N of potential temperature (gray
 249 contours) and zonal wind (filled contours). The dotted black curve denotes the 850K potential temperature
 250 surface. The contour interval for the zonal field is 10 ms⁻¹ and only winds great than 50 ms⁻¹ (red shades) and
 251 less than 0 ms⁻¹ (blue shades) are shown.

246 gravity waves at 60°N and likely at nearby latitudes as well, including the 60–65°N regions of
 247 small scale EPV features seen in Fig. 3.

252 These relatively large amplitude GWs in the stratosphere were generated by strong tropospheric
 253 northwesterly winds over Scandinavia (Fig. 6). The synoptic weather situation at this time was
 254 ideal for GW generation with a large, upper-air, high pressure system just west of the European
 255 orography. The westerly wind component in both the troposphere and stratosphere allowed wave
 256 propagation into the upper stratosphere.

257 While the 60°N zonal wind during 2021–22 was relatively strong, it did weaken during January
 258 2022, especially over the breaking gravity wave region (Fig. 7a). This weakening of the zonal wind
 259 after 11 January corresponds to the time of the peak vertical momentum flux over Europe (Fig. 7b).
 260 These strong vertical momentum fluxes are characteristic of GWs. Note that this momentum flux
 261 is greatest in the upper stratosphere and weakens above 1 hPa in the mesosphere, consistent with
 262 the GW wave structure shown in Fig. 5. While the zonal wind changes and peak momentum fluxes
 263 line up closely, the largest GW flux peak occurs about two days after the winds begin to decrease
 264 indicating that other factors in the zonal momentum budget, including planetary wave actively
 265 would be needed for a complete momentum budget.

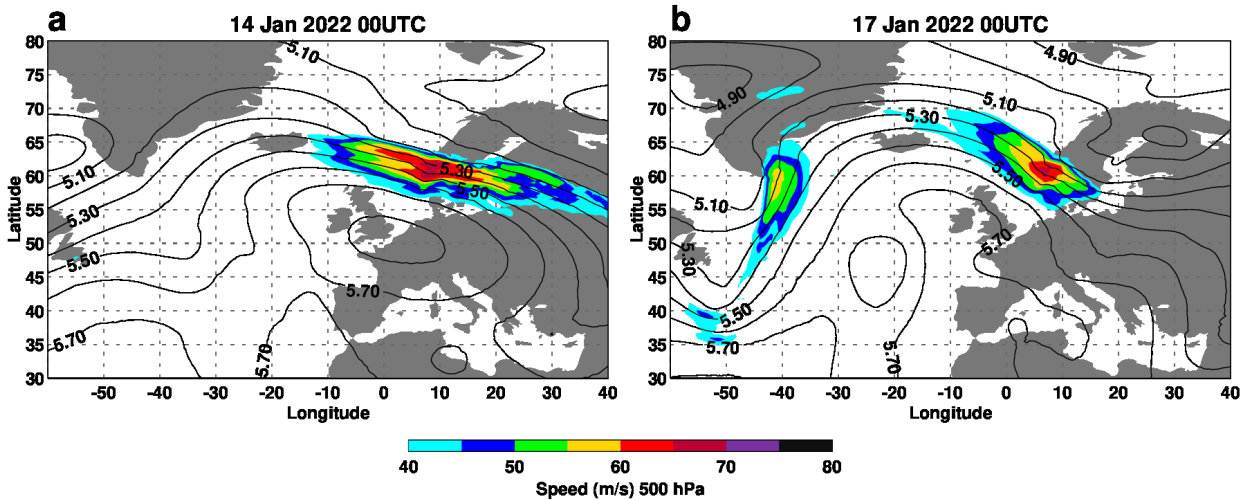
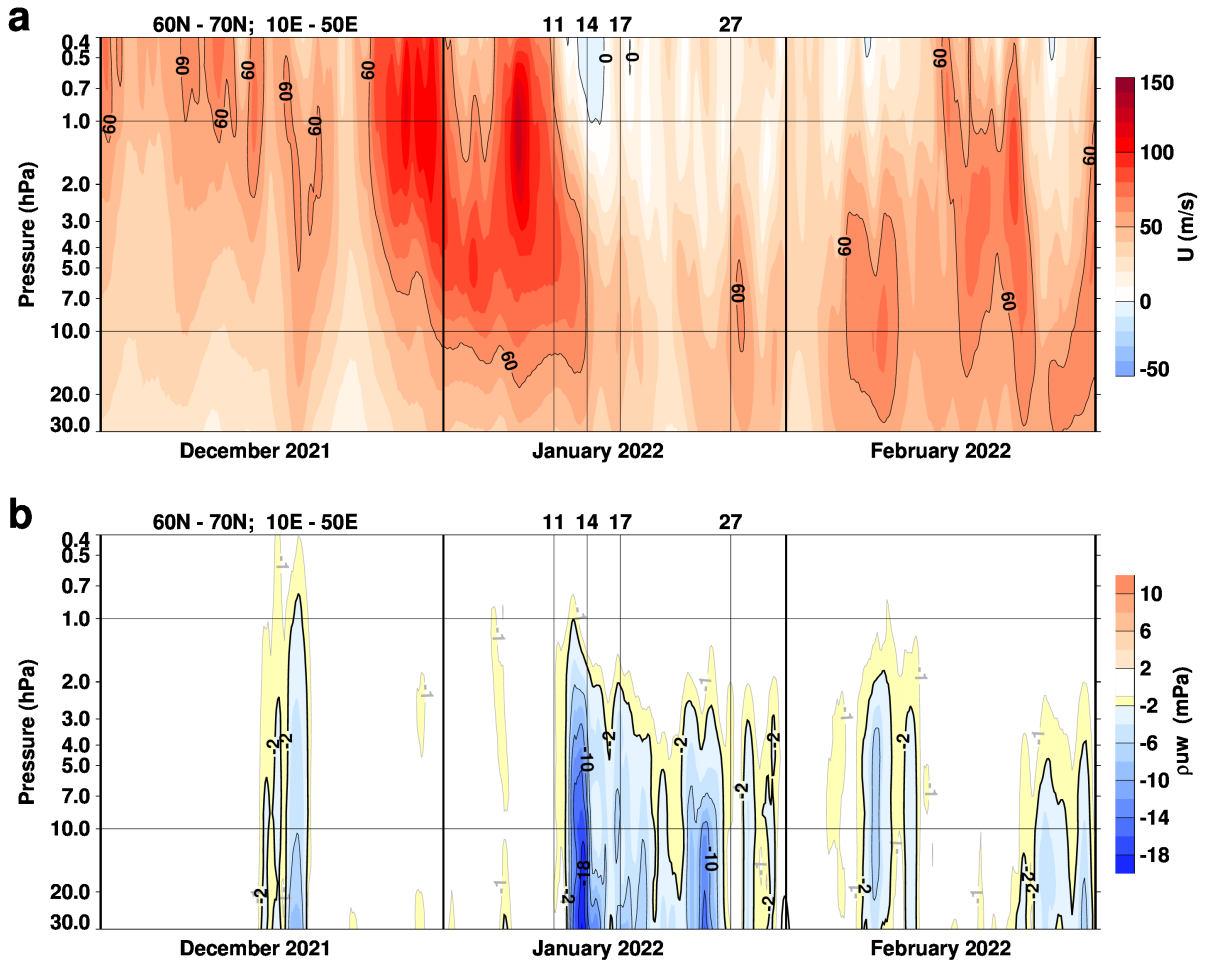


FIG. 6. Wind speed and geopotential heights at 500 hPa for a) 14 January 2022 and b) 17 January 2022.

270 The small scale GWs and mesoscale vortices as seen in Fig. 1d can be identified by the occurrence
 271 of high values of enstrophy, the square of the vorticity (Fig. 8a). There is a January 2022 burst
 272 of enstrophy coincident with the strong vertical momentum flux and these upper stratospheric
 273 strong enstrophy values continue to the end of January created by both continued GW activity
 274 and the development of the mesoscale vortices. The $\sim 1/2$ degree horizontal resolution MERRA-2
 275 system lacks the higher ($\sim 1/8$ degree) horizontal resolution of the GEOS FP system, hence the
 276 small scale features seen in the GEOS FP system's enstrophy (Fig. 8a) are not seen in MERRA-2
 277 (Fig. 8b). MERRA-2 captures some of the mesoscale vortices as seen by the slightly high than
 278 average enstrophy values during the last third of January at 10 hPa, however, it misses the very
 279 strong enstrophy values characteristic of GW breaking near mid-January.

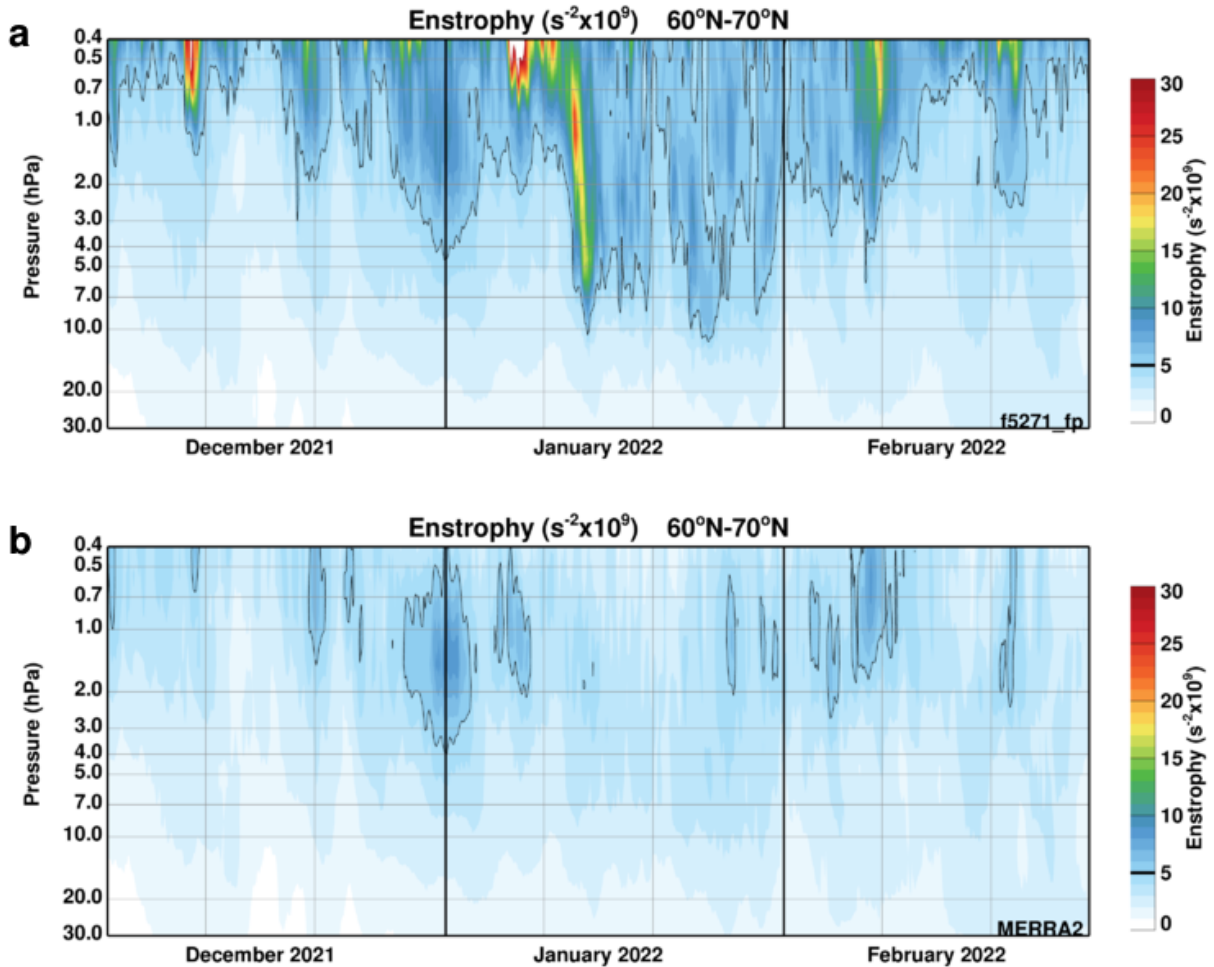
282 Note that the identification of breaking GW regions with small-scale, large positive and negative
 283 EPV fluctuations, does not imply that these are being realistically modeled as the scale of the
 284 fluctuations is near the limit of the model resolution. Rather they are taken here as a signature of
 285 GW breaking. Much higher vertical and horizontal resolution simulations are needed to accurately
 286 model the GW breaking process and its effect on EPV. Note that, while both MERRA-2 and
 287 GEOS-FP incorporate orographic GW parameterization (McFarlane 1987), these parameterized
 288 GW drag effects remained localized over the orography at an altitude just above the wind maximum
 289 but below the main resolved breaking region.



266 FIG. 7. Time (DJF) pressure (30–10 hPa) cross sections averaged over 60°–70°N and 10°–50°E for a) zonal
 267 mean zonal wind (ms^{-1}) and b) the zonal component of the density weighted vertical momentum flux (mPa).
 268 Note that in b) the dark contour is at -2 mPa, not zero, and that the the -1 mPa contour has been added (filled
 269 yellow).

290 *c. Mesoscale vortices*

291 The mesoscale vortices develop and propagate along the edge of the vortex, just poleward of the
 292 edge value delineating the low and high EPV regions. They begin to form by 14 January 2022
 293 when the EPV begins to separate from the vortex (Figs. 1b and c) and continue to develop and
 294 propagate around the vortex throughout the rest of the month. An example of the growth and
 295 propagation of the mesoscale vortices from 24–27 January is shown in figure 9.



280 FIG. 8. Time (DJF) pressure (30–10 hPa) zonal averages of enstrophy ($s^{-2} \times 10^6$) over 60–70°N for a) the
 281 GEOS FP system and b) MERRA-2.

296 EPV undulations, identified by the letters, A, B, and C can be seen on 24 January (Fig. 9a) in a
 297 region of EPV that has separated from the main high EPV region by gravity wave breaking (EPV
 298 fluctuations at the smallest resolvable scale) from Greenland to Northern Europe. Note that that
 299 these three EPV undulations can be tracked back at in time at least once around the vortex before
 300 experiencing the growth shown here after 24 January. By 25 January (Fig. 9b), the three mesoscale
 301 vortices have propagated about 90° in longitude around the main vortex. After crossing the main
 302 breaking GW region the mesoscale vortices have increased in amplitude, moving in response to the
 303 larger EPV values of the polar vortex. The mesoscale vortices, A, B, and C continue to increase in
 304 amplitude (the value of their central EPV) on the 26 January (Fig. 9c) and there is also at this time

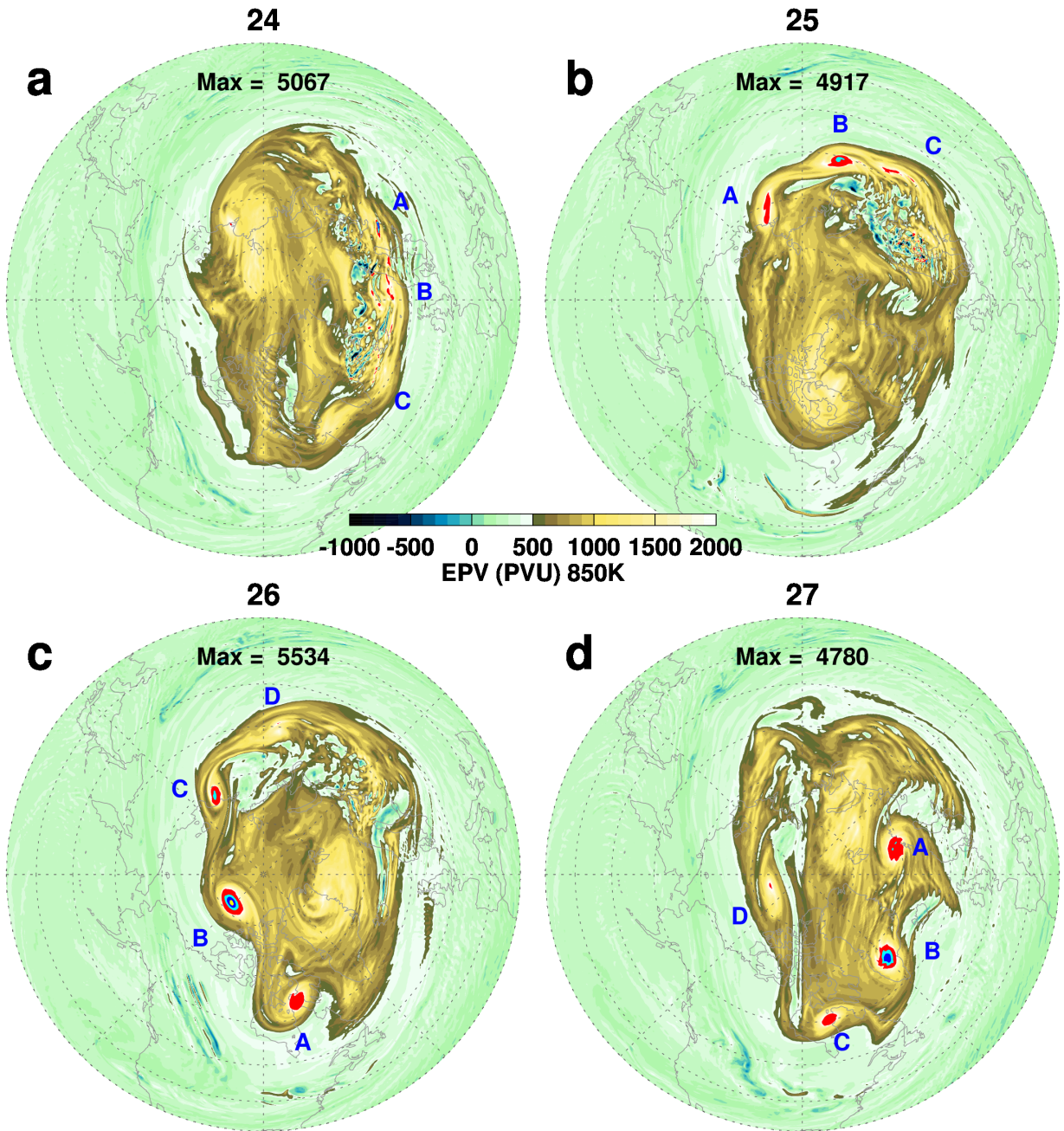
305 the identification of an additional trailing EPV region labeled D. On the last day shown, 27 January
306 (Fig. 9d), the mesoscale vortices continue their eastward propagation with A and D increasing in
307 amplitude while B and C decrease slightly in amplitude. Note that some of the mesoscale vortices
308 are associated with “breaking wave” signatures in the EPV field: A in panel c), and A, B, and C,
309 in panel d). In each of these mesoscale vortices EPV from the main vortex is being pulled off and
310 lower EPV mixed into the main vortex.

314 The trajectory of the mesoscale vortex B carried it nearly twice around the main vortex (Fig. 10).
315 After ~ 2 days increasing in strength (24–26 January), mesoscale vortex B kept its amplitude nearly
316 constant until ~ 28 January before weakening and crossing over the North Pole on 29 January and
317 eventually dissipating near Northern Europe. Mesoscale vortex B existed for about seven days
318 making its average period for a circulation around the globe approximately three and half days,
319 implying a propagation speed of 45 ms^{-1} at 70°N . This speed is close to the mean polar vortex
320 speed at this time, indicating that mesoscale vortex B has a well-conserved EPV structure during
321 this time.

327 Cross sections of mesoscale vortex B on 26 January highlight typical vertical structure of the
328 mesoscale vortices during their largest amplitude (Fig. 11). The EPV anomaly extends from ~ 10 –
329 1.5 hPa in the upper stratosphere while the potential temperature shows large perturbations starting
330 just above 20 hPa and extending through the upper stratosphere. The temperature perturbation field
331 is consistent with the potential temperature field with cool air below and warm air above. The wind
332 anomalies are located south and north of the axis of the temperature perturbation consistent with
333 the cyclonic circulation of the EPV anomalies. The strongest wind gradients (in the horizontal)
334 coincide with the strongest temperature gradients (in the vertical) consistent with the thermal wind
335 relation. The wind change across the mesoscale vortex is $\sim 80 \text{ ms}^{-1}$. The mesoscale vortices are
336 located in the upper stratosphere with little extent into the lower stratosphere.

341 *d. Resolution*

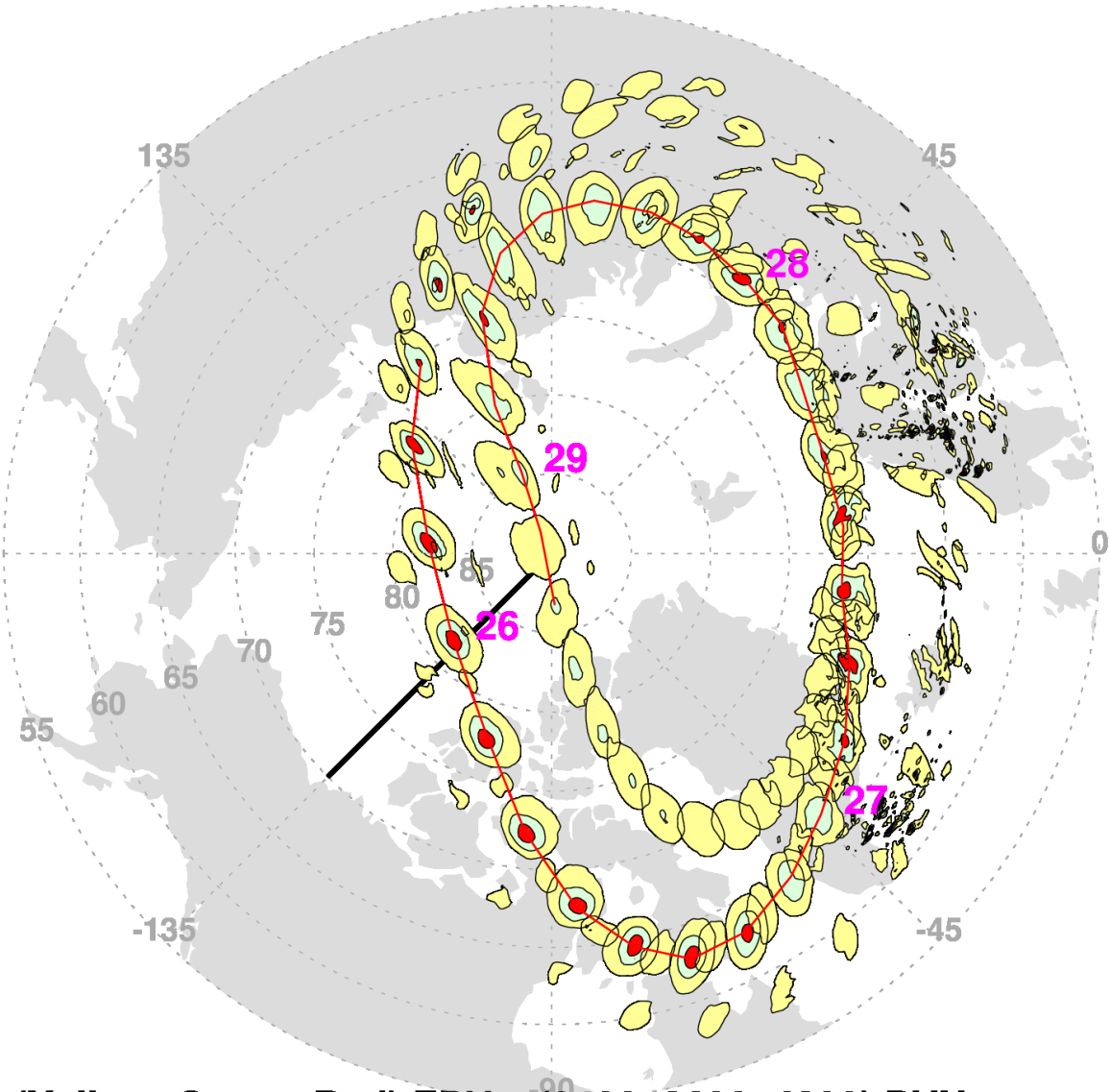
342 High horizontal resolution is needed to identify the breaking GW signature and to reveal the
343 detailed structure of the mesoscale vortices. Figure 12 shows the 850 K potential temperature
344 surface EPV field at $\sim 1/2$, $1/4$, and $1/8$ degree resolution (low, intermediate, and high). At the
345 lowest resolution, there is no evidence of breaking GWs and while there is some appearance of the



311 FIG. 9. EPV on 850K potential temperature surface for a) 24, b) 25, c) 26, and d) 27 January 2002 00UTC.
 312 The high EPV values are: red: 2000–3000 PVU, cyan: 3000–4000 PVU, blue: 4000–5000 PVU, and yellow:
 313 above 5000 PVU. Features tracked across panels are labeled A, B, C, and D.

346 EPV fluctuations at the intermediate resolution, they are much more evident at the high resolution.
 347 The well-defined mesoscale vortices only appear at the intermediate and high resolution and have

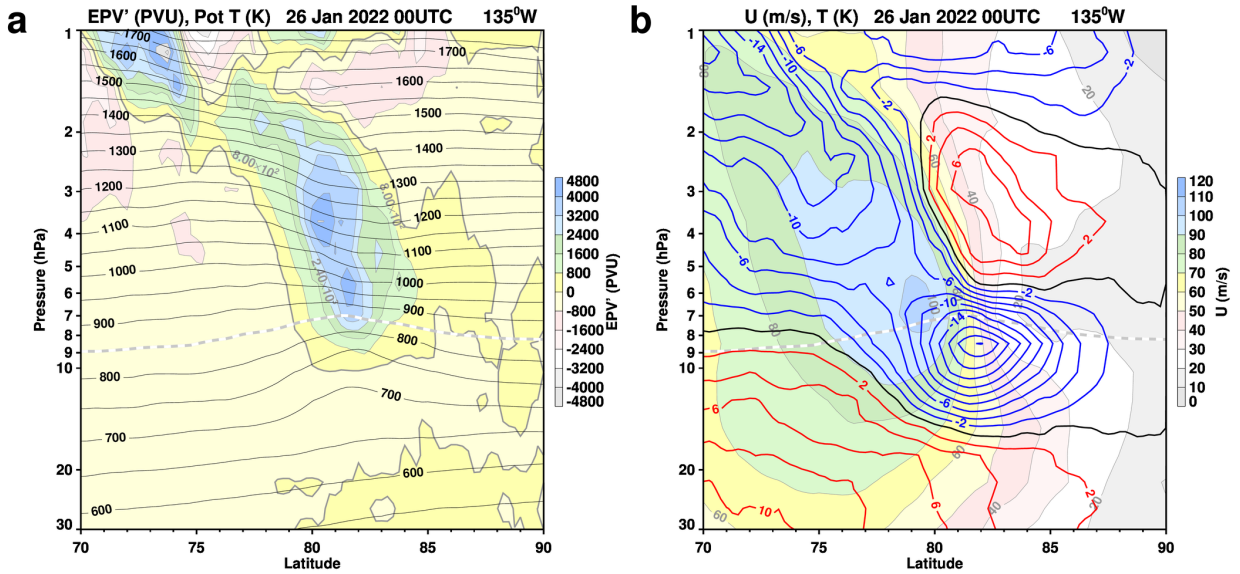
EPV 850K 24-31 Jan 2022



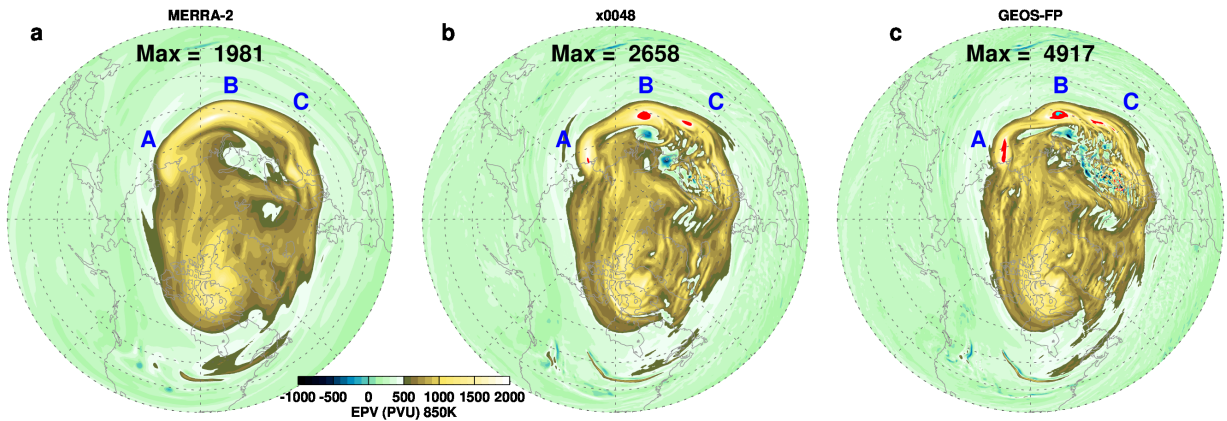
(Yellow, Green, Red) EPV > (2400, 3600, 4800) PVU

322 FIG. 10. EPV on the 850K potential temperature surface for 24–31 January 2022 contoured every three hours.
323 EPV values are colored between 2400–3600 PVU (yellow), 3600–4800 PVU (green), and greater than 4800 PVU
324 (red). The red curve connects the maximum EPV locations from 25 January 15 UTC to 29 January 6 UTC. The
325 locations of the highest EPV at 0 UTC on 26, 27, 28, and 29 January are marked. The black line denotes the
326 location of the cross section shown in Fig. 11.

348 the highest central EPV values at high resolution. All three resolutions, even the lowest, capture



337 FIG. 11. Latitude (70°–90°N) pressure (30–1 hPa) cross section at 135°W of a) EPV deviation from the
 338 zonal mean (PVU, filled contours) and potential temperature (K, black contours) and b) zonal wind (ms^{-1} , filled
 339 contours) and temperature deviation from the zonal mean (K, red positive, blue negative). The dashed gray curve
 340 denotes the 850K potential temperature.



351 FIG. 12. EPV on 850K potential temperature surface for GEOS DAS analyses at three horizontal resolutions
 352 with nominal values of a) 1/2, b) 1/4, and c) 1/8 degrees on 25 January 2022 00UTC. Contours are the same as
 353 in Fig. 9

349 the strong EPV region near A, B, and C, separated from the main vortex, creating a reversal in the
 350 latitudinal EPV gradient.

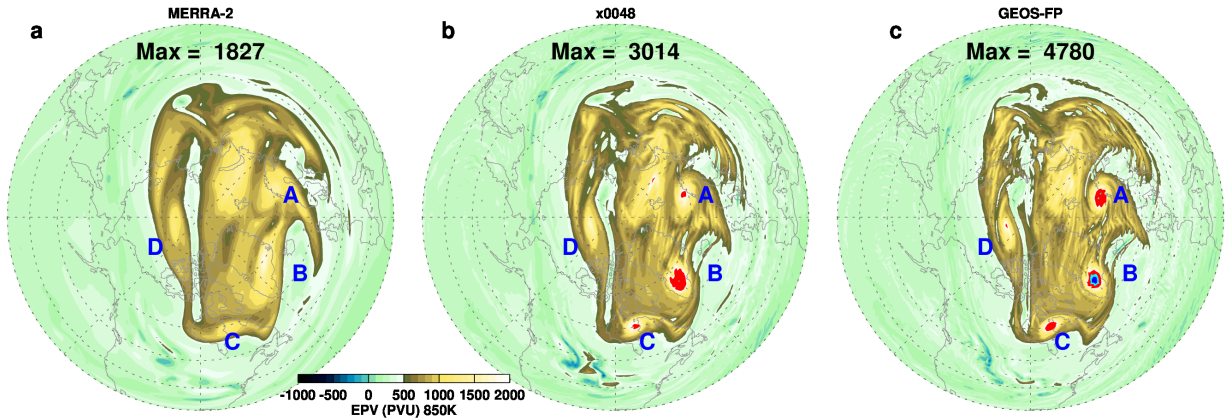


FIG. 13. Same as Fig. 12 but for 27 January 2022 00UTC

354 Later, on the 27th, the mesoscale vortices have propagated along the main vortex edge as
 355 identified by the letters (Fig. 13). They are very faint but present at low resolution, however both
 356 the intermediate and high resolutions agree well suggesting that the size of mesoscale vortices are
 357 converging with resolution and may not change much in even higher resolution systems. While
 358 the overall structure of the mesoscale vortices are similar at intermediate and high resolution, the
 359 central peak EPV values are still larger at the high resolution. Note that the maximum EPV values,
 360 occurring at mesoscale vortex “B”, increase from 3,014 at intermediate to 4,780 PVU at high
 361 resolution.

362 *e. Instability Considerations*

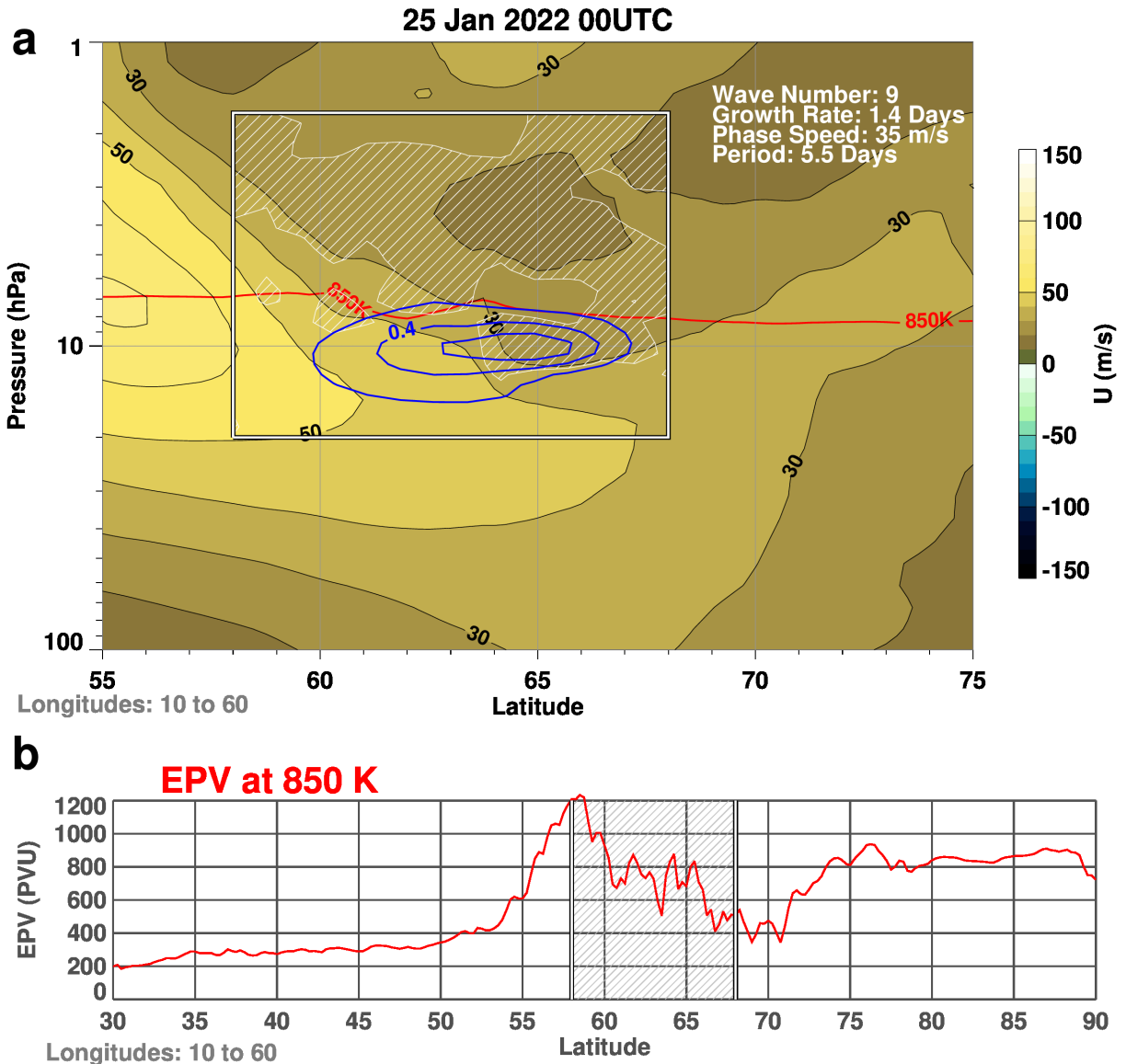
363 The formation of the mesoscale vortices from the smaller scale gravity waves presents a challenge.
 364 One possible mechanism, suggested by the reverse EPV latitudinal gradient over a substantial area,
 365 is that the mesoscale vortices are initially generated by baroclinic instability. The idea presented
 366 here is that the tropospheric generated GWs break in the stratosphere over a substantial area,
 367 creating a significant disruption of the polar vortex EPV, in turn triggering instabilities near the
 368 edge of the polar vortex. The instability then produces the mesoscale vortices. As a simple test of
 369 the instability of the flow, a linear instability model was examined for different zonal wind profiles
 370 and times. One result is shown in figure 14. Since the reversed EPV gradient is localized, the
 371 zonal winds near the GW activity, 10°–60°E, were average for the background state. The time
 372 chosen was for 25 January as the wave perturbation, especially the perturbations labeled C and D
 373 in figure 9, were still growing at that time. Other choices include time averaging of the zonal winds

374 or selecting a different longitude range. In addition the model evaluates instability over a limited
375 latitude and pressure range, here chosen to be 58°–68°N and 20–2 hPa. As in McCormack et al.
376 (2014) the boundary conditions were simply taken to be zero at all boundaries of the box. The
377 interior of the box includes a region of negative \bar{q}_y (Fig. 14a) and a reversal of the EPV gradient
378 (Fig. 14b).

379 For the above choices the fastest growing unstable wave was found at wavenumber 9, with an
380 e-folding growth rate of 1.4 days, a phase speed of 35 ms⁻¹, and a period of 5.5 days. Examining the
381 spacing of the mesoscale vortex locations of 25 January (Fig. 9b), the wavenumber 9 result is not
382 unrealistic, however the spacing between the mesoscale vortices does increase with time (Fig. 9d)
383 suggesting a smaller wavenumber. The growth rate is reasonable, however the phase speed appears
384 to be somewhat slow, leading to a period that is longer than observed when compared to the just
385 over 3-day circuit of the globe taken by the mesoscale vortex B (Fig. 9) from 26–29 January
386 (Fig. 10). The amplitude structure is confined to the lower region of the model’s domain in contrast
387 to the larger vertical extent seen in figure 11. Overall, the instability model results, while not
388 comprehensive, illustrate the potential for instability created by the breaking GW induced reversal
389 in the local EPV latitudinal gradient.

390 Note that this instability model cannot reproduce the observed growth in EPV as no diabatic
391 processes are included. In the this simple model, the EPV is rearranged to correspond to the growing
392 amplitude wave. The finite amplitude behavior of the instability requires a more sophisticated
393 model.

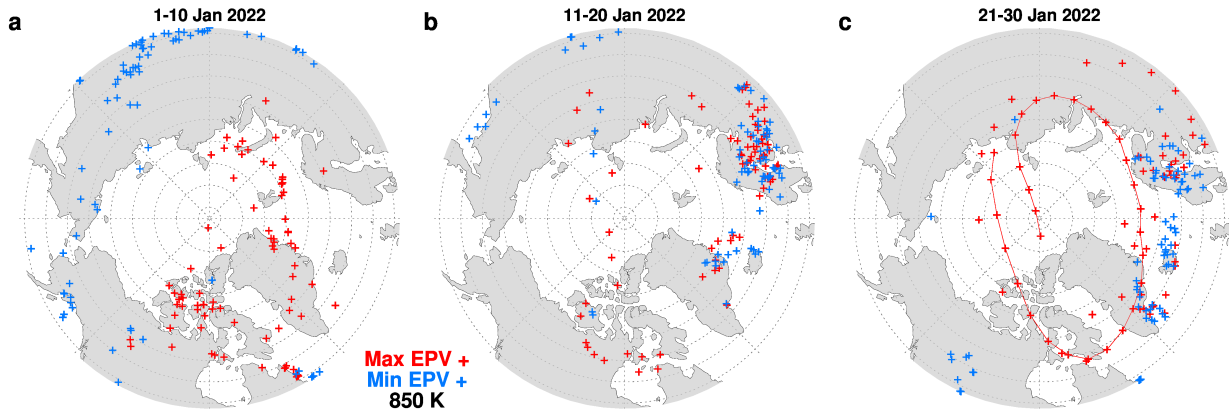
394 Another possible mechanism for the origin of the mesoscale vortices is vortex roll-up (Dritschel
395 and Polvani 1992), a shear instability occurring in some vorticity strips. These are usually seen in
396 EPV filaments well outside of the main polar vortex that are pulled off the polar vortex by breaking
397 planetary waves (McIntyre and Palmer 1983). This differs from the situation in January 2022
398 where the EPV is split while still aligned with the main vortex flow, however the end result is
399 an isolated strip of EPV and hence, potential shear instability. It is likely that a combination of
400 instability mechanisms is at play during the complex dynamics of January 2022.



401 FIG. 14. a) zonal mean wind averaged over 10–60° E (filled contours), the region of negative \bar{q}_y (shaded), the
 402 850K potential temperature (red contour), the non-dimensional fastest growing wave amplitude (blue contours),
 403 and b) EPV (PVU) averaged over 10–60° E as a function of latitude. The box in a) and the shaded region in b)
 404 denotes the stability model domain used

405 **4. Summary and Conclusions**

406 This study based on the 12 km resolution DAS revealed two new features in the EPV analysis:
 407 high and low fluctuations at the smallest model scale associated with GW breaking, and high values
 408 associated with mesoscale vortices along the edge of the polar vortex. In this case both types of

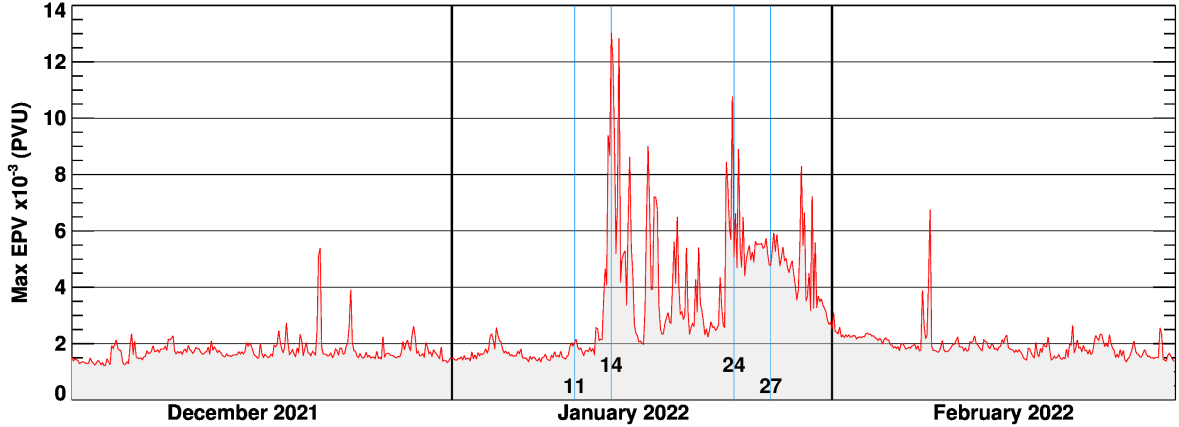


420 FIG. 15. The locations of the maximum (red) and minimum (blue) values of EPV on the 850K potential
 421 temperature surface at each analysis time for a) 1–10, b) 11–20, and c) 21–30 January 2022. The minimum
 422 locations are restricted to the area shown on the map projection. The red curve connects the maximum EPV
 423 locations from 25 January 15 UTC to 29 January 9 UTC.

409 anomalous EPV values were related, as the persistent GW breaking created a region of reversed
 410 EPV gradient that triggered the formation of the mesoscale vortices.

411 The location of NH maximum and minimum values of 850K EPV at each analysis time provides
 412 a convenient overview of the breaking GW regions during January 2022 (Fig. 15). During the
 413 first ten-days the highest EPV values are at the highest latitudes and lowest EPV values are at the
 414 lower latitudes, consistent with the NH climatological poleward gradient of EPV. By the middle of
 415 January, however, the distribution has changed with maximum and minimum EPV locations close
 416 together over Northern Europe, the Greenland coast, and Iceland. These indicate regions of strong
 417 GW breaking as seen in the EPV field. Later in January, these "salt and pepper" patterns continue
 418 with the addition of several days (25–29 January) when the maximum EPV value was associated
 419 with a propagating mesoscale vortex.

424 The maximum value of 850K EPV can characterize the overall NH winter of 2021–22 with a
 425 nominal maximum value of just under 2000 PVU for most of the winter season (Fig. 16). Starting
 426 on 14 January, values that are 5× higher appear, coincident with the appearance of GW breaking.
 427 These spikes continue for the remainder of the month with the addition of a more consistent in
 428 time bulge of high EPV, a signature of the persistent mesoscale vortices. These dramatic events
 429 are mostly over by the start of February.



430 FIG. 16. Maximum EPV value on the 850K potential temperature surface as a function of time (10^{-3} PVU).
 431 11, 14, 24, and 27 January 2022 are denoted by blue vertical lines.

432 How realistic are these very high EPV values seen in DAS? It is difficult to be definitive at this time.
 433 The very smallest scale EPV fluctuations, occurring in association with GW breaking, are likely
 434 greatly influenced by the limited model resolution. However, higher horizontal resolution leads to
 435 more sharply defined mesoscale vortices with higher central EPV values (Fig. 13). Comparison
 436 of the evolution of the mesoscale vortices in FP with the lower resolution MERRA-2 EPV fields
 437 (Fig. 13) shows that at lower resolution the FP mesoscale vortices can be identified as a smoothed
 438 version of the higher resolution system. If the wind change is approximately the same across a
 439 mesoscale vortex but the doubled horizontal resolution allows for a doubling of the gradient, then
 440 the EPV values can be expected to double as well.

441 Only one potential mechanism for the creation of the mesoscale vortices was investigated here.
 442 Other, perhaps very different, mechanisms are possible. Additionally, the simple linear instability
 443 model examined here lacks the ability to follow the perturbation to finite amplitude and to grow
 444 the EPV values, a distinctive feature of the vortices that needs explanation. Consider the equation
 445 for EPV in isentropic coordinates (Andrews et al. 1987, Equ 3.8.5):

$$\tilde{D}P = (\sigma a \cos \phi)^{-1} [-(X \cos \phi)_\phi + Y_\lambda - Q_\lambda v_\theta + Q_\phi u_\theta \cos \phi] + PQ_\theta - QP_\theta,$$

446 where \tilde{D} is the time derivative following the isentropic flow, P is potential vorticity, σ is the
 447 isentropic density, a is the radius of the earth, ϕ is latitude, λ is longitude, θ is potential temperature,
 448 X and Y are the latitude and longitude frictional forces, u and v are the velocity components, and
 449 Q is the diabatic forcing. Neglecting frictional forces and scaling for quasi-geostrophic motion
 450 (Haynes and McIntyre 1987), the equation becomes:

$$\tilde{D}P \approx PQ_{\theta} - QP_{\theta}$$

451 While time averaged diabatic heating terms are typically saved in the DAS output, the quadratic
 452 terms are not save so additional output would be useful. In addition, the non-geostrophic terms
 453 may contribute to the mesoscale vortices. It should be noted that, along with the mesoscale high
 454 EPV, some regions of mesoscale low EPV stand out. This is especially noticeable in Fig. 12b, the
 455 intermediate resolution experiment, near “B” and “C”, suggesting that isentropic redistribution of
 456 EPV is playing a role rather than problematic model numerics in creating the high EPV features
 457 and supporting the concept of rearrangement of EPV as part of the development of the mesoscale
 458 vortices.

459 The different orientation and scale of EPV fluctuations from the associated GWs needs further
 460 investigation. Detailed three dimensional models of GW breaking (Fritts et al. 2009a,b) resolve
 461 the small scale, rapid, variability created during the breaking process and the generation of EPV
 462 by breaking GWs has been recently modeled by Waite and Richardson (2023). These studies
 463 suggest that “spanwise”, that is disturbances along the wavefront, commonly develop, however
 464 relating these to global scale EPV is not yet clear. While we have focused on a single NH winter
 465 in which planetary wave activity was relatively weak to highlight the GWs and their effects on the
 466 polar vortex, it is likely that breaking GWs in the mid to upper stratosphere are fairly common and
 467 routinely contribute to mixing at the edge of the polar vortex.

468 In future studies we plan to examine other years when high resolution FP DAS fields are available
 469 along with results from test model and assimilation experiments at higher horizontal and vertical
 470 resolution. More evaluation of the amount of mixing along the polar vortex edge by the mesoscale
 471 vortices is also needed. Even though the scale of these vortices is relatively small, the amount of
 472 mixing could be substantial as these mesoscale vortices form where tracer gradients are large. In
 473 addition, since some evidence of the mesoscale vortices can be found at low resolution such as

474 in Fig. 13a, it may be possible to develop a climatology of when these events occur by searching
475 the longer time record of the lower resolution MERRA-2 DAS. Such a climatology would provide
476 information of the role played by the mesoscale vortices in observed climatological stratospheric
477 tracer distributions.

478 *Acknowledgments.* This work was supported by NASA MAP (Grant NNG17HP01C) and ACPMAP
479 programs (Grants 80NSSC19K1005, NNH18ZDA001N). Support for MJA provided by NASA
480 Grant Nos. 80NSSC23K0519 and 80NSSC23K1311. Resources supporting this work were pro-
481 vided by the NASA High-End Computing (HEC) Program through the NASA Center for Climate
482 Simulation (NCCS) at Goddard Space Flight Center.

483 *Data availability statement.* The GEOS data used in this study/project have been provided by
484 the Global Modeling and Assimilation Office (GMAO) at NASA Goddard Space Flight Cen-
485 ter. The Forward Processing (FP) DAS output are archived at <https://portal.nccs.nasa.gov/datashare/gmao/geos-fp/das> and the system used in this study is labeled f5271_fp.
487 The MERRA-2 data is available from the NASA's Goddard Earth Sciences Data and In-
488 formation Services Center (GES DISC, <https://disc.gsfc.nasa.gov/datasets?project=MERRA-2>).
489 Specific MERRA-2 data sets used are contained in the references. The AIRS brightness
490 temperatures are available from https://datapub.fz-juelich.de/slcs/airs/gravity_waves/html/view_2022_014.html The IDL (Interactive Data Language) code used for the
492 quasi-geostrophic instability model is archived at https://gmao.gsfc.nasa.gov/gmaoftp/larrycoy/instability_code/stability_package.pro. The x0048 DAS fields used to
493 construct intermediate resolution EPV fields on 25 and 27 January 2022 are archived at
494 https://gmao.gsfc.nasa.gov/gmaoftp/larrycoy/mesoscale_vortices.

496 **References**

- 497 Achatz, U., and Coauthors, 2024: Atmospheric gravity waves: Processes and parameterization.
498 *Journal of the Atmospheric Sciences*, **81** (2), 237–262, [https://doi.org/10.1175/JAS-D-23-0210.](https://doi.org/10.1175/JAS-D-23-0210.1)
499 1, URL <https://journals.ametsoc.org/view/journals/atsc/81/2/JAS-D-23-0210.1.xml>.
- 500 Albers, J. R., and T. Birner, 2014: Vortex preconditioning due to planetary and gravity
501 waves prior to sudden stratospheric warmings. *Journal of the Atmospheric Sciences*, **71** (11),
502 4028 – 4054, <https://doi.org/10.1175/JAS-D-14-0026.1>, URL <https://journals.ametsoc.org/view/journals/atsc/71/11/jas-d-14-0026.1.xml>.
- 504 Alexander, M. J., 2010: Gravity waves in the stratosphere. *The Stratosphere: Dynamics, Transport,*
505 *and Chemistry*, L. M. Polvani, A. H. Sobel, and D. W. Waugh, Eds., American Geophysical

506 Union, Washington, DC, 109–122.

507 Andrews, D. G., J. R. Holton, and C. B. Leovy, 1987: *Middle Atmosphere Dynamics*. Academic
508 Press, 489 pp.

509 Arnold, N. P., W. M. Putman, and S. R. Freitas, 2020: Impact of resolution and parameterized
510 convection on the diurnal cycle of precipitation in a global nonhydrostatic model. *Journal of
511 the Meteorological Society of Japan. Ser. II*, **98 (6)**, 1279–1304, [https://doi.org/10.2151/jmsj.
512 2020-066](https://doi.org/10.2151/jmsj.2020-066).

513 Butchart, N., 2022: The stratosphere: a review of the dynamics and variability. *Weather and
514 Climate Dynamics*, **3 (4)**, 1237–1272, <https://doi.org/10.5194/wcd-3-1237-2022>, URL <https://wcd.copernicus.org/articles/3/1237/2022/>.

516 Dritschel, D. G., and L. M. Polvani, 1992: The roll-up of vorticity strips on the surface of a sphere.
517 *J. Fluid Mech.*, **234**, 47–69.

518 Fritts, D. C., and M. J. Alexander, 2003: Gravity wave dynamics and effects
519 in the middle atmosphere. *Reviews of Geophysics*, **41 (1)**, [https://doi.org/https://doi.
520 org/10.1029/2001RG000106](https://doi.org/https://doi.org/10.1029/2001RG000106), URL [https://agupubs.onlinelibrary.wiley.com/doi/abs/10.1029/
521 2001RG000106](https://agupubs.onlinelibrary.wiley.com/doi/abs/10.1029/2001RG000106), <https://agupubs.onlinelibrary.wiley.com/doi/pdf/10.1029/2001RG000106>.

522 Fritts, D. C., L. Wang, J. Werne, T. Lund, and K. Wan, 2009a: Gravity wave instability dynamics
523 at high reynolds numbers. part i: Wave field evolution at large amplitudes and high frequencies.
524 *Journal of the Atmospheric Sciences*, **66 (5)**, 1126 – 1148, [https://doi.org/https://doi.org/10.1175/
525 2008JAS2726.1](https://doi.org/https://doi.org/10.1175/2008JAS2726.1), URL <https://journals.ametsoc.org/view/journals/atsc/66/5/2008jas2726.1.xml>.

526 Fritts, D. C., L. Wang, J. Werne, T. Lund, and K. Wan, 2009b: Gravity wave instability dynamics at
527 high reynolds numbers. part ii: Turbulence evolution, structure, and anisotropy. *Journal of the At-
528 mospheric Sciences*, **66 (5)**, 1149 – 1171, [https://doi.org/https://doi.org/10.1175/2008JAS2727.
529 1](https://doi.org/https://doi.org/10.1175/2008JAS2727.1), URL <https://journals.ametsoc.org/view/journals/atsc/66/5/2008jas2727.1.xml>.

530 Gelaro, R., and Coauthors, 2017: The Modern-Era Retrospective Analysis for Research and
531 Applications, Version 2 (MERRA-2). *Journal of Climate*, **30 (14)**, 5419–5454, [https://doi.org/
532 10.1175/JCLI-D-16-0758.1](https://doi.org/10.1175/JCLI-D-16-0758.1), URL <https://doi.org/10.1175/JCLI-D-16-0758.1>, [https://doi.org/
533 10.1175/JCLI-D-16-0758.1](https://doi.org/10.1175/JCLI-D-16-0758.1).

- 534 GMAO, 2015a: Global Modeling and Assimilation Office, inst3 3d asm Nv: MERRA-2 3D Assim-
535 ilated Meteorological Fields 3-hourly (model level, 0.625x0.5L42), version 5.12.4. Greenbelt,
536 MD, USA: Goddard Space Flight Center Distributed Active Archive Center (GSFC DAAC),
537 accessed June 2016, <https://doi.org/10.5067/WWQSXQ8IVFW8>.
- 538 GMAO, 2015b: Global Modeling and Assimilation Office, instM 3d asm Np: MERRA-2 3D
539 IAU State, Meteorology Monthly Averaged 3-hourly (p-coord, 0.625x0.5L42), version 5.12.4.
540 Greenbelt, MD, USA: Goddard Space Flight Center Distributed Active Archive Center (GSFC
541 DAAC), accessed June 2016, <https://doi.org/10.5067/2E096JV59PK7>.
- 542 Haynes, P. H., and M. E. McIntyre, 1987: On the evolution of vorticity and po-
543 tential vorticity in the presence of diabatic heating and frictional or other forces.
544 *Journal of Atmospheric Sciences*, **44** (5), 828 – 841, [https://doi.org/https://doi.org/10.](https://doi.org/https://doi.org/10.1175/1520-0469(1987)044<0828:OTEOVA>2.0.CO;2)
545 [1175/1520-0469\(1987\)044<0828:OTEOVA>2.0.CO;2](https://doi.org/https://doi.org/10.1175/1520-0469(1987)044<0828:OTEOVA>2.0.CO;2), URL [https://journals.ametsoc.org/view/](https://journals.ametsoc.org/view/journals/atsc/44/5/1520-0469_1987_044_0828_oteova_2_0_co_2.xml)
546 journals/atsc/44/5/1520-0469_1987_044_0828_oteova_2_0_co_2.xml.
- 547 Haynes, P. H., and M. E. McIntyre, 1990: On the conservation and impermeability theorems for
548 potential vorticity. *Journal of Atmospheric Sciences*, **47** (16), 2021 – 2031, [https://doi.org/https://](https://doi.org/https://doi.org/10.1175/1520-0469(1990)047<2021:OTCAIT>2.0.CO;2)
549 [doi.org/10.1175/1520-0469\(1990\)047<2021:OTCAIT>2.0.CO;2](https://doi.org/https://doi.org/10.1175/1520-0469(1990)047<2021:OTCAIT>2.0.CO;2), URL [https://journals.ametsoc.](https://journals.ametsoc.org/view/journals/atsc/47/16/1520-0469_1990_047_2021_otcait_2_0_co_2.xml)
550 [org/view/journals/atsc/47/16/1520-0469_1990_047_2021_otcait_2_0_co_2.xml](https://journals/atsc/47/16/1520-0469_1990_047_2021_otcait_2_0_co_2.xml).
- 551 Hoffmann, L., M. J. Alexander, C. Clerbaux, A. W. Grimsdell, C. I. Meyer, T. Rößler, and
552 B. Tournier, 2014: Intercomparison of stratospheric gravity wave observations with AIRS
553 and IASI. *Atmospheric Measurement Techniques*, **7** (12), 4517–4537, [https://doi.org/10.5194/](https://doi.org/10.5194/amt-7-4517-2014)
554 [amt-7-4517-2014](https://doi.org/10.5194/amt-7-4517-2014), URL <https://amt.copernicus.org/articles/7/4517/2014/>.
- 555 Holt, L. A., M. J. Alexander, L. Coy, C. Liu, A. Molod, W. Putman, and S. Pawson, 2017: An eval-
556 uation of gravity waves and gravity wave sources in the southern hemisphere in a 7 km global cli-
557 mate simulation. *Quarterly Journal of the Royal Meteorological Society*, **143** (707), 2481–2495,
558 <https://doi.org/https://doi.org/10.1002/qj.3101>, URL [https://rmets.onlinelibrary.wiley.com/doi/](https://rmets.onlinelibrary.wiley.com/doi/abs/10.1002/qj.3101)
559 [abs/10.1002/qj.3101](https://rmets.onlinelibrary.wiley.com/doi/pdf/10.1002/qj.3101), <https://rmets.onlinelibrary.wiley.com/doi/pdf/10.1002/qj.3101>.
- 560 Hoskins, B. J., M. E. McIntyre, and A. W. Robertson, 1985: On the use and significance
561 of isentropic potential vorticity maps. *Quarterly Journal of the Royal Meteorological Soci-*
562 *ety*, **111** (470), 877–946, <https://doi.org/https://doi.org/10.1002/qj.49711147002>, URL <https://doi.org/https://doi.org/10.1002/qj.49711147002>, URL <https://doi.org/https://doi.org/10.1002/qj.49711147002>.

563 //rmets.onlinelibrary.wiley.com/doi/abs/10.1002/qj.49711147002, <https://rmets.onlinelibrary.wiley.com/doi/pdf/10.1002/qj.49711147002>.

565 Matthias, V., and M. Ern, 2018: On the origin of the mesospheric quasi-stationary planetary
566 waves in the unusual arctic winter 2015/2016. *Atmos. Chem. Phys.*, **18**, 4803–4815, URL
567 <https://doi.org/10.5194/acp-18-4803-2018>.

568 McCormack, J. P., L. Coy, and W. Singer, 2014: Intraseasonal and interannual variability
569 of the quasi 2 day wave in the northern hemisphere summer mesosphere. *Journal of Geo-*
570 *physical Research: Atmospheres*, **119** (6), 2928–2946, [https://doi.org/https://doi.org/10.1002/](https://doi.org/https://doi.org/10.1002/2013JD020199)
571 [2013JD020199](https://doi.org/https://doi.org/10.1002/2013JD020199), URL <https://agupubs.onlinelibrary.wiley.com/doi/abs/10.1002/2013JD020199>,
572 <https://agupubs.onlinelibrary.wiley.com/doi/pdf/10.1002/2013JD020199>.

573 McFarlane, N. A., 1987: The effect of orographically excited gravity wave drag on the general
574 circulation of the lower stratosphere and troposphere. *J. Atmos. Sci.*, **44**, 1775–1800.

575 McIntyre, M. E., and T. N. Palmer, 1983: Breaking planetary waves in the stratosphere. *Nature*,
576 **305**, 593–600.

577 Nash, E. R., P. A. Newman, J. E. Rosenfield, and M. R. Schoeberl, 1996: An objective
578 determination of the polar vortex using Ertel's potential vorticity. *Journal of Geophysi-*
579 *cal Research: Atmospheres*, **101** (D5), 9471–9478, [https://doi.org/https://doi.org/10.1029/](https://doi.org/https://doi.org/10.1029/96JD00066)
580 [96JD00066](https://doi.org/https://doi.org/10.1029/96JD00066), URL <https://agupubs.onlinelibrary.wiley.com/doi/abs/10.1029/96JD00066>, <https://agupubs.onlinelibrary.wiley.com/doi/pdf/10.1029/96JD00066>.

582 Okui, H., C. J. Wright, N. P. Hindley, E. J. Lear, and K. Sato, 2023: A comparison of stratospheric
583 gravity waves in a high-resolution general circulation model with 3-d satellite observations.
584 *Journal of Geophysical Research: Atmospheres*, **128** (13), e2023JD038795, [https://doi.org/](https://doi.org/https://doi.org/10.1029/2023JD038795)
585 [https://doi.org/10.1029/2023JD038795](https://doi.org/https://doi.org/10.1029/2023JD038795), URL [https://agupubs.onlinelibrary.wiley.com/doi/abs/](https://agupubs.onlinelibrary.wiley.com/doi/abs/10.1029/2023JD038795)
586 [10.1029/2023JD038795](https://agupubs.onlinelibrary.wiley.com/doi/abs/10.1029/2023JD038795), e2023JD038795 2023JD038795, <https://agupubs.onlinelibrary.wiley.com/doi/pdf/10.1029/2023JD038795>.

588 Putman, W. M., and S.-J. Lin, 2007: Finite-volume transport on various cubed-sphere grids.
589 *Journal of Computational Physics*, **227** (1), 55–78, [https://doi.org/https://doi.org/10.1016/j.jcp.](https://doi.org/https://doi.org/10.1016/j.jcp.2007.07.022)
590 [2007.07.022](https://doi.org/https://doi.org/10.1016/j.jcp.2007.07.022), URL <https://www.sciencedirect.com/science/article/pii/S0021999107003105>.

- 591 Sato, K., R. Yasui, and Y. Miyoshi, 2018: The momentum budget in the stratosphere, mesosphere,
592 and lower thermosphere. Part I: Contributions of different wave types and in situ generation of
593 Rossby waves. *J. Atmos. Sci.*, **75**, 3613–3633, URL <https://doi.org/10.1175/JAS-D-17-0336.1>.
- 594 Shibuya, R., and K. Sato, 2019: A study of the dynamical characteristics of inertia–gravity
595 waves in the antarctic mesosphere combining the PANSY radar and a non-hydrostatic general
596 circulation model. *Atmospheric Chemistry and Physics*, **19** (5), 3395–3415, <https://doi.org/10.5194/acp-19-3395-2019>, URL <https://acp.copernicus.org/articles/19/3395/2019/>.
- 598 Siskind, D. E., S. D. Eckermann, J. P. McCormack, L. Coy, K. W. Hoppel, and N. L. Baker, 2010:
599 Case studies of the mesospheric response to recent minor, major, and extended stratospheric
600 warmings. *J. Geophys. Res.*, **115** (D00N03), <https://doi.org/doi:10.1029/2010JD014114>.
- 601 Smith, A. K., 1996: Longitudinal variations in mesospheric winds: Evidence for gravity wave
602 filtering by planetary waves. *J. Atmos. Sci.*, **53** (8), 1156–1173.
- 603 Stevens, B., and Coauthors, 2019: DYAMOND: the DYnamics of the Atmospheric general
604 circulation Modeled On Non-hydrostatic Domains. *Prog Earth Planet Sci*, **6** (61), URL
605 <https://doi.org/10.1186/s40645-019-0304-z>.
- 606 Waite, M. L., and N. Richardson, 2023: Potential vorticity generation in breaking gravity
607 waves. *Atmosphere*, **14** (5), <https://doi.org/10.3390/atmos14050881>, URL <https://www.mdpi.com/2073-4433/14/5/881>.
- 609 Watanabe, S., and S. Miyahara, 2009: Quantification of the gravity wave forcing of the mi-
610 grating diurnal tide in a gravity wave–resolving general circulation model. *J. Geophys. Res.*,
611 **114** (D07110), doi:10.1029/2008JD011218.
- 612 Zhu, Y., R. Todling, and N. Arnold, 2022: Observation impact and information retention in
613 the lower troposphere of the gmao geos data assimilation system. *Monthly Weather Review*,
614 **150** (8), 2187 – 2205, <https://doi.org/https://doi.org/10.1175/MWR-D-21-0334.1>, URL <https://journals.ametsoc.org/view/journals/mwre/150/8/MWR-D-21-0334.1.xml>.
- 615